remote sensing

Technical Note

Multi-Antenna Global Navigation Satellite System/Inertial Measurement Unit Tight Integration for Measuring Displacement and Vibration in Structural Health Monitoring

Wujiao Dai [1,*], Xin Li [1], Wenkun Yu [1], Xuanyu Qu [2] and Xiaoli Ding [2]

[1] School of Geosciences and Info-Physics, Central South University, Changsha 410083, China
[2] Department of Land Surveying & Geo-Informatics, The Hong Kong Polytechnic University, Hung Hom, Kowloon, Hong Kong, China; xl.ding@polyu.edu.hk (X.D.)
* Correspondence: wjdai@csu.edu.cn

Abstract: Large-scale engineering structures deform and vibrate under the influence of external forces. Obtaining displacement and vibration is crucial for structural health monitoring (SHM). Global navigation satellite system (GNSS) and inertial measurement unit (IMU) are complementary and widely used in SHM. In this paper, we propose an SHM scheme where IMU and multi-antenna GNSS are tightly integrated. The phase centers of multiple GNSS antennas are transformed into the IMU center, which increases the observation redundancy and strengthens the positioning model. To evaluate the performance of tight integration of IMU and multiple GNSS antennas, high-rate vibrational signals are simulated using a shaking table, and the errors of horizontal displacement of different positioning schemes are analyzed using recordings of a high-precision ranging laser as the reference. The results demonstrate that applying triple-antenna GNSS/IMU integration for measuring the displacement can achieve an accuracy of 2.6 mm, which is about 33.0% and 30.3% superior than the accuracy achieved by the conventional single-antenna GNSS-only and GNSS/IMU solutions, respectively.

Keywords: multi-antenna GNSS; GNSS/IMU; tight integration; structural health monitoring

Citation: Dai, W.; Li, X.; Yu, W.; Qu, X.; Ding, X. Multi-Antenna Global Navigation Satellite System/Inertial Measurement Unit Tight Integration for Measuring Displacement and Vibration in Structural Health Monitoring. *Remote Sens.* **2024**, *16*, 1072. https://doi.org/10.3390/rs16061072

Academic Editor: Baocheng Zhang

Received: 19 February 2024
Revised: 15 March 2024
Accepted: 15 March 2024
Published: 18 March 2024

1. Introduction

For large-scale structures, serious structural damage may occur when vibrating deformation induced by external loads (such as traffic and winds) exceeds the designed bearing capacity. Accurate deformation information is a prerequisite for timely alerts to prevent unnecessary casualties and losses. SHM is a technology for obtaining deformation information and estimating the health condition and the structural characteristics of civil structures and infrastructures [1,2]. On this basis, an SHM strategy first intends to measure responses such as displacements over time, and then obtain insightful information about the current or unknown condition of a civil structure by computational techniques either in time domain or in frequency domain [3,4]. Various types of sensor devices such as linear variable differential transformers, optical fiber sensors, smartphones, vision cameras, and radars are used in SHM to measure the displacement responses, but dynamic deformation monitoring widely adopts GNSS and accelerometers for SHM non-stop or with high periodicity but not requiring gluing/embedding sensors into the structure [5–8]. The RTK-GNSS can achieve a subcentimeter-level measurement accuracy, and it is often selected for structural displacement estimation of large-scale structures such as long-span bridges and high-rise buildings, which usually have at least centimeter-level displacements [9–11]. However, the accuracy of GNSS positioning is typically limited due to environmental perturbations such as occlusion, diffraction, and reflection. In addition, the GNSS-based monitoring method is insensitive to high-frequency vibration signals because the measurement noise is relatively large [12]. The accelerometer method can obtain high-accuracy dynamical displacements over short time periods through the double integration of acceleration measurements. However, significant cumulative errors are ultimately present when the accelerometer is applied to monitor long-period quasi-static displacements [13].

GNSS and accelerometers are complementary and therefore have been commonly integrated in monitoring applications. For example, Meng et al. [14] successfully identified a peak vibration frequency of 10.05 Hz of Nottingham Wilford Bridge by using an GNSS/accelerometer integrated system. Kim et al. [15] combined GPS RTK with an accelerometer in monitoring Yeongjong Grand Bridge and achieved a displacement accuracy of 2 mm in the vertical direction. Xin et al. [16] integrated a strong motion accelerometer with GNSS PPP for seismic deformation monitoring. The root-mean-square error (RMSE) of the difference with respect to the reference was 2 mm, with a cross-correlation coefficient of 0.99. Although GNSS/accelerometer integration has been widely validated in previous studies, the tilt of the accelerometer can cause baseline errors and distort the captured peak amplitude of the displacement signal [14,16].

In addition to displacement, rotational deformation is another critical piece of information for structural health monitoring. Although the accelerometer can measure the rotational deformation by sensing changes in gravitational acceleration [17], the accuracy of accelerometer-derived rotation is typically limited because accelerometers measure specific forces that involve gravitational and vibrational acceleration. To separate the different types of acceleration and finally determine the rotational deformation, it is necessary to use gyroscopes [18]. Rossi et al. [19] corrected the impact of rotation on GNSS/accelerometer monitoring results using rotation information recorded using an inertial measurement unit (IMU). The RMSE of the corrected displacement monitoring results was reduced by half to about 1–2 mm. de Alteriis et al. [20] designed a low-cost and real-time monitoring device that integrated GNSS and Micro Electro Mechanical System (MEMS) IMU. Experimental results showed that the system was able to estimate position and attitude under high-frequency vibrations, and the monitoring results were in good agreement with the fiber-optic sensors. Geng et al. [21] implemented a seismic monitoring system with six degrees of freedom by integrating an accelerometer, gyroscope, and GNSS. In a waveform simulation experiment of the 2010 MW 7.2 EI Mayor-Cucapah earthquake, the displacement obtained using the proposed method achieved an accuracy 68% higher than that obtained from the traditional accelerometer/GNSS integration.

Most previous studies of integrated GNSS/IMU deformation monitoring are based on single-antenna GNSS. Although improved accuracy and robustness have been reported, there are still some obvious limitations of single-antenna GNSS/IMU. For example, the GNSS signal environment in deformation monitoring is typically complex, which worsens the GNSS signal quality and ultimately the positioning accuracy. Moreover, the motion of the monitored structures is generally limited, resulting in a low attitude observability, especially in the heading direction [22,23]. The accumulation of attitude errors eventually affects the monitoring accuracy, especially when low-cost IMUs are used [24]. Multi-antenna GNSS offers a solution to this problem. Double-difference carrier phases are formed between multiple GNSS antennas to estimate inter-antenna baselines. When carrier phase ambiguities are fixed, the baselines can be accurately inverted to attitude information [25]. Zhang et al. [26] evaluated the positioning performance of the traditional single-antenna and dual-antenna GNSS/IMU. They reported that the dual-antenna GNSS/IMU achieved mm level positioning accuracy, which was about 50% higher than the single-antenna GNSS/IMU. Li et al. [27] applied the length constraints of lever arms in multi-antenna GNSS/IMU for monitoring the settlement of high-speed railway, and achieved a positioning accuracy of 1–2 mm. However, multi-antenna GNSS/IMU integration has been rarely studied in structural deformation monitoring.

In this paper, we propose a tight integration of multi-antenna GNSS and IMU for vibration monitoring. The GNSS observations are tightly coupled to the IMU by transforming their phase centers to the IMU center. Thus, the integration reduces the number of unknown parameters, enhances the geometric strength of the model, and increases the observability of attitude errors. To evaluate the performance of the proposed method, different types of vibrational signals are simulated using a shaking table and a laser rangefinder recording as a reference. Section 2 presents the mathematical model of the tight integration of multi-antenna GNSS and IMU, including the measurement model and the system model. In Section 3, the experimental configuration, results, and analysis are described. Section 4 concludes this work.

2. Methods

2.1. Multi-Antenna GNSS/IMU Tight Integration Measurement Model

The measurement model of GNSS/IMU tight integration can be expressed as:

$$\delta \boldsymbol{z} = \boldsymbol{H}\delta \boldsymbol{x} + \boldsymbol{\epsilon}\,,\ \boldsymbol{\epsilon} \sim N(\boldsymbol{0},\ \boldsymbol{R}) \tag{1}$$

where $\delta\{\cdot\}$ indicates the correction for a variable; $\delta \boldsymbol{z}$ denotes the measurement correction vector that is the difference between GNSS observations (including carrier phases and pseudorange rates) and those derived from IMU; $\boldsymbol{H}$ is the design matrix; $\delta \boldsymbol{x}$ is the state correction vector; $\boldsymbol{\epsilon}$ represents the observation noise vector; and $\boldsymbol{R}$ corresponds to the covariance matrix of observations. The state vector $\boldsymbol{x}$ is:

$$\boldsymbol{x} = \begin{bmatrix} \boldsymbol{r}^T & \boldsymbol{v}^T & \boldsymbol{\psi}^T & \boldsymbol{b}_a{}^T & \boldsymbol{b}_g{}^T & \boldsymbol{n}^T \end{bmatrix}^T \tag{2}$$

where $\boldsymbol{r}$ is the three-dimensional position vector, taking the IMU reference center as the reference point of the platform; $\boldsymbol{v}$ and $\boldsymbol{\psi}$, respectively, indicate the velocity and attitude of the platform; $\boldsymbol{b}_a$ and $\boldsymbol{b}_g$ denote the biases of accelerometer and gyroscope, respectively; and $\boldsymbol{n}$ corresponds to the ambiguities of double-difference carrier phases.

When composing the measurement model for the multi-antenna GNSS and IMU tight integration system, one rover antenna is chosen as the primary antenna and the others are used as auxiliary antennas. The double-difference observation equation is formed between the primary antenna and the reference station, which introduces an absolute position for the whole system. At the same time, the double-difference observation equations are also formed between the primary antenna and the auxiliary antennas to adequately exploit the redundant observations from multiple antennas. The double-difference carrier phase $\boldsymbol{z}_{ij}$ and pseudorange rate $\dot{\boldsymbol{z}}_{ij}$ between antenna i and antenna j can be written as:

$$\begin{cases} \boldsymbol{z}_{ij} = \boldsymbol{A}_i \boldsymbol{r}_i - \boldsymbol{A}_j \boldsymbol{r}_j + \boldsymbol{\Lambda}_{ij} n + \boldsymbol{\epsilon}_{ij} \\ \dot{\boldsymbol{z}}_{ij} = \boldsymbol{A}_i \boldsymbol{v}_i - \boldsymbol{A}_j \boldsymbol{v}_j + \dot{\boldsymbol{\epsilon}}_{\boldsymbol{ij}} \end{cases} \tag{3}$$

where $\boldsymbol{r}_i$ and $\boldsymbol{v}_i$ are, respectively, the position and velocity of antenna i; $\boldsymbol{A}_i$ stands for an $m \times 3$ line-of-sight matrix of between-satellite single-difference at antenna i, where m is the difference between the total number of satellites observed and the number of satellite systems employed; $\boldsymbol{\Lambda}_{ij}$ is a diagonal matrix with non-zero elements being the carrier phase wavelengths of the corresponding satellites; and $\boldsymbol{\epsilon}_{ij}$ denotes the double-difference observation noise. The position vector $\boldsymbol{r}_i$ and velocity vector $\boldsymbol{v}_i$ of antenna i can be transformed to the platform position vector $\boldsymbol{r}$ and velocity vector $\boldsymbol{v}$ at the IMU center through the lever-arm vector and rotation matrix [28]:

$$\boldsymbol{r}_i = \boldsymbol{r} + \boldsymbol{C}\boldsymbol{l}_i \tag{4}$$

$$\boldsymbol{v}_i = \boldsymbol{v} + \boldsymbol{C}(\boldsymbol{\Omega}_\omega \boldsymbol{l}_i) + \boldsymbol{\Omega}_e \boldsymbol{C}\boldsymbol{l}_i,\ \boldsymbol{\Omega}_\omega = [\boldsymbol{\omega}\times] \tag{5}$$

where $\boldsymbol{C}$ is the direction cosine matrix, i.e., the rotation matrix; $\boldsymbol{l}_i$ stands for the lever-arm vector of antenna i; $\boldsymbol{\Omega}_\omega$ indicates the skew-symmetric matrix of three-dimensional angular rate obtained by IMU, i.e., $[\boldsymbol{\omega}\times]$; $[\cdot\times]$ represents a skew-symmetric operator; and $\boldsymbol{\Omega}_e$ denotes the skew-symmetric matrix of earth angle rotation speed vector. Inserting (4) and (5) into (3) yields the double-difference carrier phase and pseudorange rate equations expressed by the position vector and velocity vector of the IMU center:

$$\begin{cases} z_{ij} = A_{ij}r + A_i C l_i - A_j C l_j + \Lambda_{ij} n + \epsilon_{ij} \\ \dot{z}_{ij} = A_{ij}v + A_i(C\Omega_\omega l_i + \Omega_e C l_i) - A_j(C\Omega_\omega l_j + \Omega_e C l_j) + \dot{\epsilon}_{ij} \end{cases} \tag{6}$$

where A_{ij} is the difference of A_i and A_j, i.e., $A_{ij} = A_i - A_j$. Given that

$$\delta(Cl_i) = [(Cl_i)\times]\delta\psi \tag{7}$$

$$\delta(C\Omega_\omega l_i + \Omega_e C l_i) = [(C\Omega_\omega l_i - \Omega_e C l_i)\times]\delta\psi \tag{8}$$

the design matrix of (1) can be expressed in terms of submatrix as:

$$H_{ij} = \begin{bmatrix} A_{ij} & \mathbf{0}_{m\times 3} & H_{r\psi} & \mathbf{0}_{m\times 3} & \mathbf{0}_{m\times 3} & \Lambda_{ij} \\ \mathbf{0}_{m\times 3} & A_{ij} & H_{v\psi} & \mathbf{0}_{m\times 3} & H_{vb} & \mathbf{0}_{m\times n} \end{bmatrix} \tag{9}$$

where $\mathbf{0}_{m\times n}$ stands for an $m \times n$ matrix with zero elements. The specific expressions of $H_{r\psi}$, $H_{v\psi}$, H_{vb} are:

$$H_{r\psi} = A_i[(Cl_i)\times] - A_j[(Cl_j)\times] \tag{10}$$

$$H_{v\psi} = A_i[(C\Omega_\omega l_i - \Omega_e C l_i)\times] - A_j[(C\Omega_\omega l_j - \Omega_e C l_j)\times] \tag{11}$$

$$H_{vb} = A_i C[l_i\times] - A_j C[l_j\times] \tag{12}$$

Note that $A_j = \mathbf{0}$ when j indicates an external base station with known coordinates.

2.2. Multi-Antenna GNSS/IMU Tight Integration System Model

The system model of the integration system of GNSS and IMU can be expressed as:

$$\delta\dot{x}(t) = F(t)\delta x(t) + G(t)w(t) \tag{13}$$

where $F(t)$ is the transition matrix of state vector; $G(t)$ stands for the process noise mapping matrix; and $w(t)$ indicates the process noise vector. The reference coordinate frame adopted in this paper is the Earth-Centered Earth-Fixed (ECEF). The sensor bias errors of the accelerometer and gyroscope are modeled as first-order Gauss–Markov stochastic processes. After the discretization of (13) with update interval τ, the state propagation equation can be rewritten as:

$$\delta x_{k+1}^- = \Phi_k \delta x_k + w_k \tag{14}$$

where x_{k+1}^- is a prediction of state vector of time t_{k+1} based on the one of time t_k, i.e., x_k, and the "−" indicates a quantity has not been updated using the latest observation; and Φ_k and w_k are the transition matrix of state vector and the process noise matrix from time t_k to time t_{k+1}, respectively. The first order approximation of Φ_k can be obtained as follows:

$$\Phi \approx \begin{bmatrix} I_3 & I_3\tau & \mathbf{0}_3 & \mathbf{0}_3 & \mathbf{0}_3 & \mathbf{0}_{3\times n} \\ F_{vp}\tau & I_3 - 2\Omega_e\tau & [-(Cf)\times] & C\tau & \mathbf{0}_3 & \mathbf{0}_{3\times n} \\ \mathbf{0}_3 & \mathbf{0}_3 & I_3 - \Omega_e\tau & \mathbf{0}_3 & C\tau & \mathbf{0}_{3\times n} \\ \mathbf{0}_3 & \mathbf{0}_3 & \mathbf{0}_3 & F_{ba} & \mathbf{0}_3 & \mathbf{0}_{3\times n} \\ \mathbf{0}_3 & \mathbf{0}_3 & \mathbf{0}_3 & \mathbf{0}_3 & F_{bg} & \mathbf{0}_{3\times n} \\ \mathbf{0}_{n\times 3} & \mathbf{0}_{n\times 3} & \mathbf{0}_{n\times 3} & \mathbf{0}_{n\times 3} & \mathbf{0}_{n\times 3} & I_n \end{bmatrix} \tag{15}$$

$$F_{vp} = -\frac{2\gamma r^T}{r_{es}|r|} \tag{16}$$

$$\begin{cases} F_{ba} = diag\left(e^{-\tau/T_{c,\,ba}}\right) \\ F_{bg} = diag\left(e^{-\tau/T_{c,\,bg}}\right) \end{cases} \tag{17}$$

where r_{es} is the geocentric radius on the Earth surface; γ indicates the gravity vector; and $T_{c,\,ba}$ and $T_{c,\,bg}$ are the correlation time of accelerometer and gyroscope, respectively, which can be obtained using Allan variance analysis.

Figure 1 shows the flowchart of the tight integration of multi-antenna GNSS and IMU. First, raw observations from multiple antennas are processed, with one primary antenna and the others auxiliary. The double-difference observation equations are formed between the antennas and the reference station (equally, between a selected primary antenna and the reference station, as well as the auxiliary antennas). Relative positioning is performed based on the double-difference observations to obtain the position, velocity, and attitude information of the integrated system. The GNSS-derived information can be used for the initial alignment of the IMU when the ambiguities are fixed. The attitude initialization can also be done using INS self-alignment, with the accelerometer leveling to calculate pitch and roll angles, and gyro-compass to calculate heading angles. The position, velocity, and attitude information of the integrated system can then be updated based on the IMU output. The angular rate of the gyro output is first used to update the attitude, based on which the specific force output from the accelerometer is transformed, and then the velocity and position information are updated. Finally, the equations of state and measurements of the integrated system are formulated, and the Kalman filter is applied to estimate the position, velocity, and attitude of the IMU center at each epoch, together with feedback corrections for sensor errors.

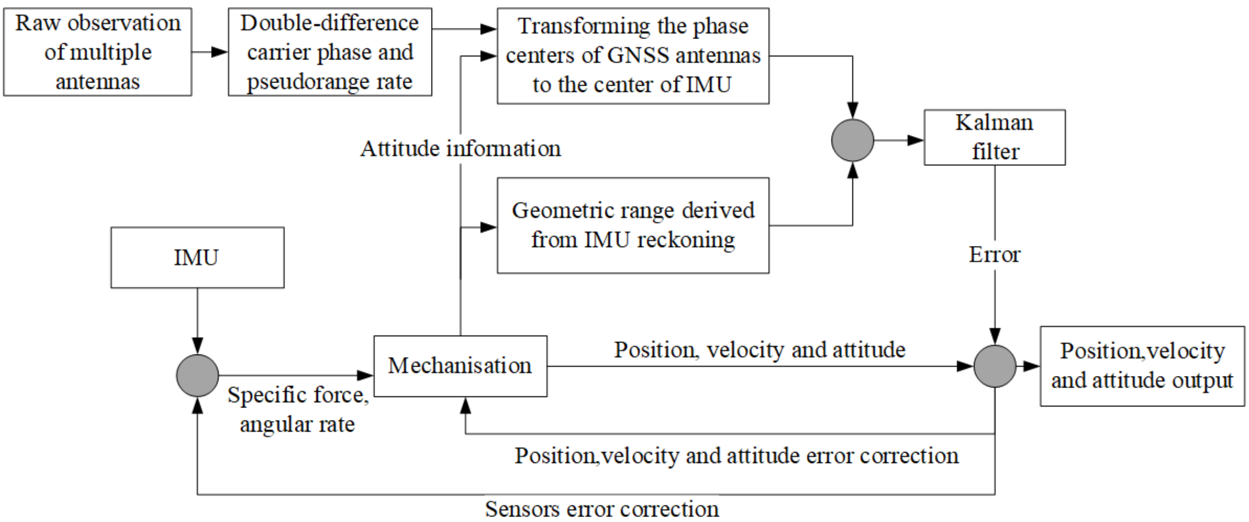

Figure 1. Flowchart of the tight integration of multi-antenna GNSS and IMU.

3. Experiments and Analysis

To assess the performance of the tight integration of multi-antenna GNSS and IMU for vibration deformation monitoring, a simulation vibration test was conducted on 13 November 2023 on a half-open platform on the 6th floor of Hong Kong Polytechnic University. Figure 2a illustrates the environment of the experimental site. The monitoring accuracy of integration schemes of different antennas and IMU were analyzed, and the vibration displacement information recorded using a laser rangefinder with a ranging accuracy of 0.01 mm, and a sampling rate of 20 Hz was used as the reference. Figure 2b shows the instrument deployment for the vibration experiment. A shaking table was fixed on a tripod. A rigid triangular platform with one IMU and four GNSS antennas was mounted on the table, and the length of inter-antenna baselines was 1 m. In deformation monitoring, the observability of attitude errors is typically low because of the limited dynamics (including rotation and acceleration) of the deforming objects. The three-dimensional attitude can be determined using at least three non-collinear antennas. Therefore, this study adopts the triple-antenna triangle configuration to strengthen the GNSS/IMU positioning model so that the estimation of parameters such as attitude and IMU biases can be enhanced. A

Leica GR25 GNSS geodetic receiver was attached to antenna 2, two Trimble R12 GNSS geodetic receivers were placed for rover antennas 1 and 3, respectively, and a Trimble Net R9 geodetic receiver was used for the base station. We use the configuration of the three non-collinear antennas to enhance the three-dimensional attitude determination, considering that the observability of attitude is typically low due to the limited dynamics of the deforming objects. The base station was located on the roof of the building at a distance of about 50 m. The GNSS sampling rate was 20 Hz. The IMU adopted was iXBLUE ATLANS-C, which has triple-axis accelerometers and gyroscopes, and a self-contained GNSS receiver for time synchronization (the corresponding antenna was installed at the center of the triangular platform). The error characteristics of IMU were estimated using Allan variance analysis [29], as shown in Table 1.

Figure 2. Experiment setup. (**a**) Environment of experimental site; (**b**) setup of experimental equipment.

Table 1. Error characteristics of IMU.

Error Characteristics	Accelerometer	Gyroscope
Bias instability	0.0241 mg	0.0084 deg/h
Correlation time	477 s	2957 s
Random walk	0.046 mg/sqrt (Hz)	0.0035 deg/sqrt (h)

A suite of C++ libraries was developed for the data processing, where IMU records are tightly integrated with GNSS observations in double-difference relative kinematic positioning. The double-difference observation equations are formed between the primary antenna and the reference station, as well as the auxiliary antennas. GPS and BDS observations were used for positioning in the experiments. In short baselines, the frequency-dependent ionospheric delays are considerably canceled, and therefore only single-frequency (L1/B1) observations were used in the experiment to reduce the computation of high-rate data. The cut-off angle was set to 10 degrees, and observations were weighted using an elevation-based cosine function.

Figure 3 shows the sky distribution of the observed GPS and BDS satellites, where G denotes the GPS satellite and C the BDS satellite. It can be seen that during the test, about 8–9 GPS satellites and 16–17 BDS satellites were observed by Antennas 1, 3, and the base station. Satellite signals from the southeast direction with low elevation angles (below 30 degrees) were not received due to the blocking of nearby buildings (Figure 2). Note that Antenna 2 could observe 9 GPS satellites but only 8 BDS-2 satellites because the firmware of the receiver was outdated.

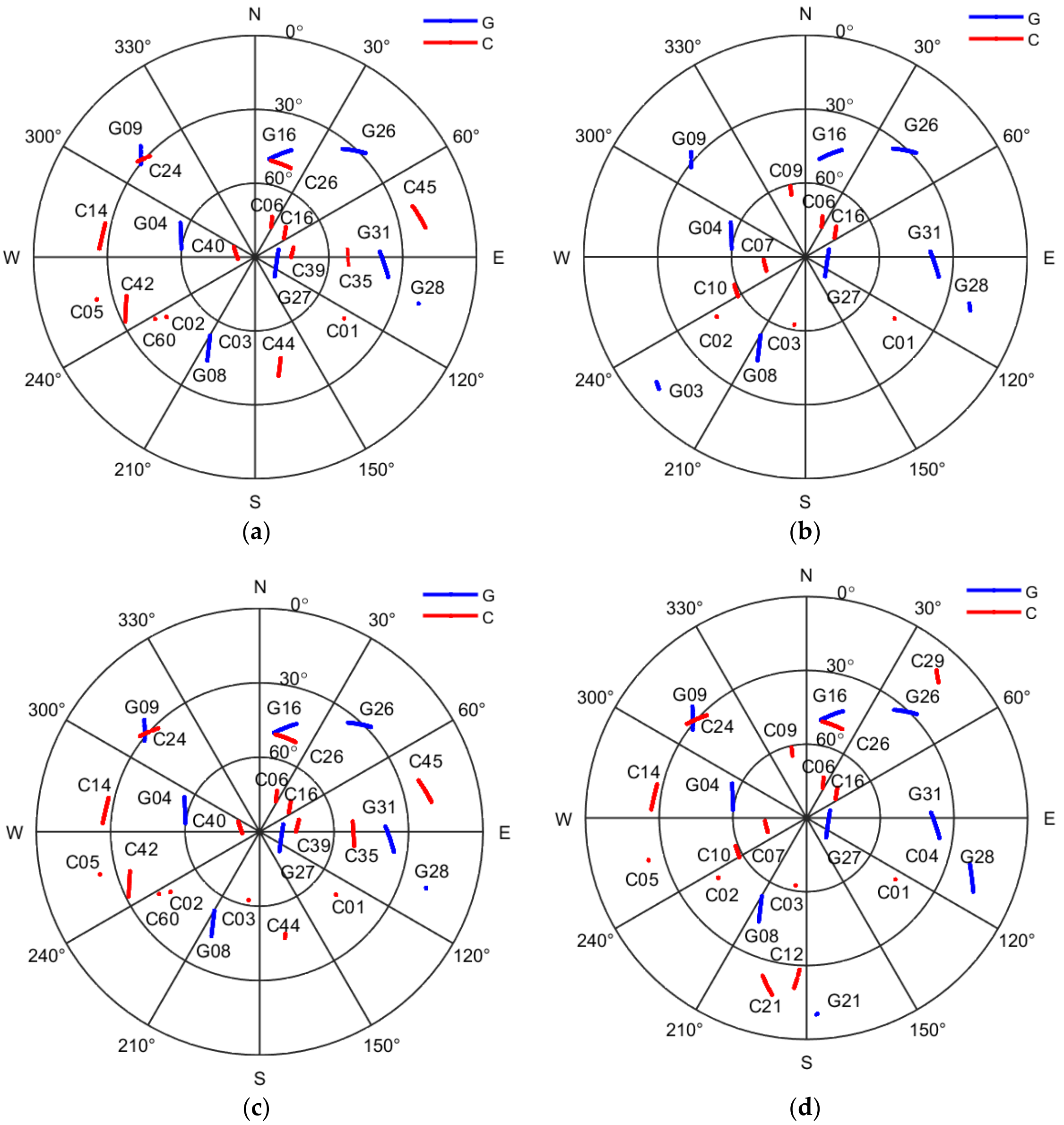

Figure 3. Sky map of GPS and BDS satellites observed by different antennas. (**a**) Antenna 1; (**b**) Antenna 2; (**c**) Antenna 3; and (**d**) antenna of base station.

Table 2 lists eleven positioning schemes that were tested in our experiment, including three single-antenna GNSS-only schemes, one triple-antenna GNSS-only scheme (using the average of the three single-antenna GNSS-only solutions), and seven GNSS/IMU integration schemes with different antennas.

Figure 4 shows the 2D horizontal displacement time series recorded with the laser rangefinder, and the horizontal displacements derived by relative positioning using schemes G1, G2, and G3. As shown in Figure 4a, the shaking table was first kept stationary for about 10 min, which was referred to as Period 1, then generated two 1 min horizontal vibrations with frequencies of 0.50 Hz and 0.67 Hz and amplitudes of 19 mm and 17 mm, respectively. After that, a vibration with a mixed frequency of 0.11 Hz and 0.34 Hz was loaded to the shaking table for about 4 min. Then the shaking table generated a vibration with a frequency of 0.80 Hz and an amplitude of 15 mm. At last, the shaking table returned to the original position in 4 min and then repeated the vibration process. The whole vibration process was named Period 2. We can see that all eight vibration events were successfully captured by the three single-antenna GNSS-only schemes. In both Period

1 and Period 2, the G2 solution was slightly nosier than those of G1 and G3, mainly because of the relatively fewer satellites tracked by Antenna 2 (see also Figure 3).

Table 2. Experimental positioning schemes.

Positioning Scheme	Antennas	Integrated with IMU
G1	Antenna 1	No
G2	Antenna 2	No
G3	Antenna 3	No
G123	Antenna 1, 2, and 3	No
GI1	Antenna 1	Yes
GI2	Antenna 2	Yes
GI3	Antenna 3	Yes
GI12	Antenna 1 and 2	Yes
GI13	Antenna 1 and 3	Yes
GI23	Antenna 2 and 3	Yes
GI123	Antenna 1, 2, and 3	Yes

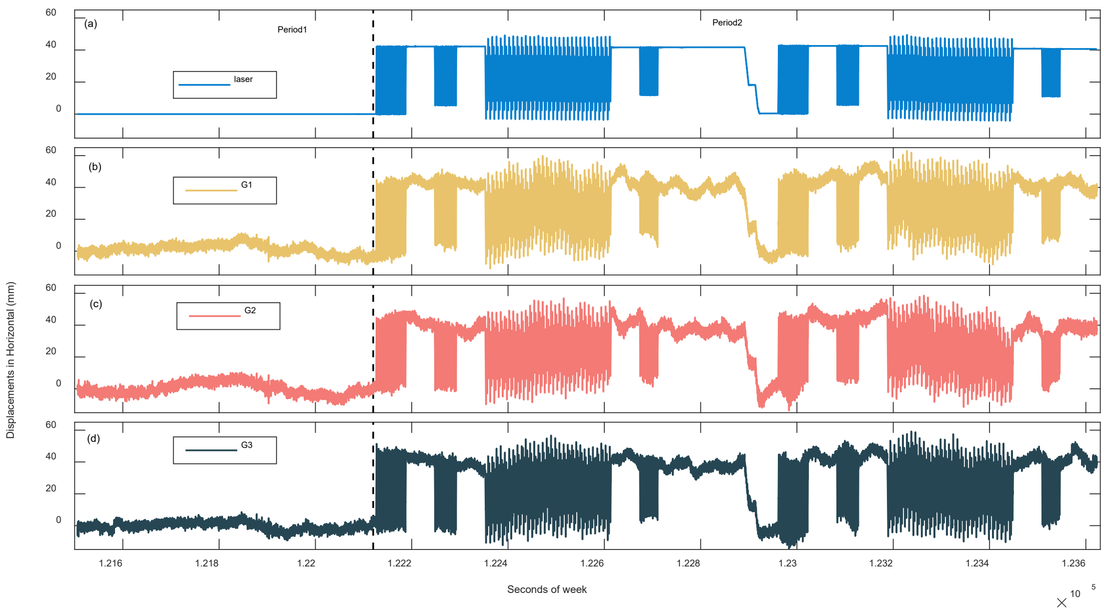

Figure 4. Horizontal displacement time series of the (**a**) ranging laser and (**b**–**d**) single-antenna GNSS-only positioning schemes.

Figure 5 shows the errors of the horizontal displacement of different positioning schemes. We can see from Figure 5a that during Period 1, the positioning errors of single-antenna GNSS-only schemes (i.e., G1, G2, and G3) fluctuate within about 10 mm, and the fluctuations become larger (within 20 mm) in Period 2, maybe due to the coupling of GNSS systematic errors and vibrations. The results of G2 are nosier than those of G1 and G3; for instance, large deviations are present in G2 during 123,400–123,600 s, perhaps due to relatively weaker geometry and undetected outliers. Integrating IMU with single-antenna GNSS data significantly reduces the positioning errors, which become obviously smaller and smoother. However, many low-frequency fluctuations remain visible in the error time series. This implies that the dominant influence is highly correlated with the single-antenna GNSS-only solution errors (Figure 5a). The benefit of multiple antennas, as can be seen in GI12, GI13, GI23, and GI123 solutions, is evident when observations from more GNSS antennas are gradually integrated (Figure 5b–d). Low-frequency systematic errors are mitigated and many error peaks are reduced (see, e.g., the period of 123,400–123,600 s). This demonstrates that the integration of multiple antennas can enhance the geometry of positioning. Typically, scheme G123, that is based on the average of three corresponding single-antenna GNSS-only solutions (Figure 5d), can achieve similar performance with dual-antenna GNSS/IMU integration (Figure 5c). And the triple-antenna GNSS/IMU solution GI123 further reduces the positioning errors compared with G123 by adding IMU (Figure 5d).

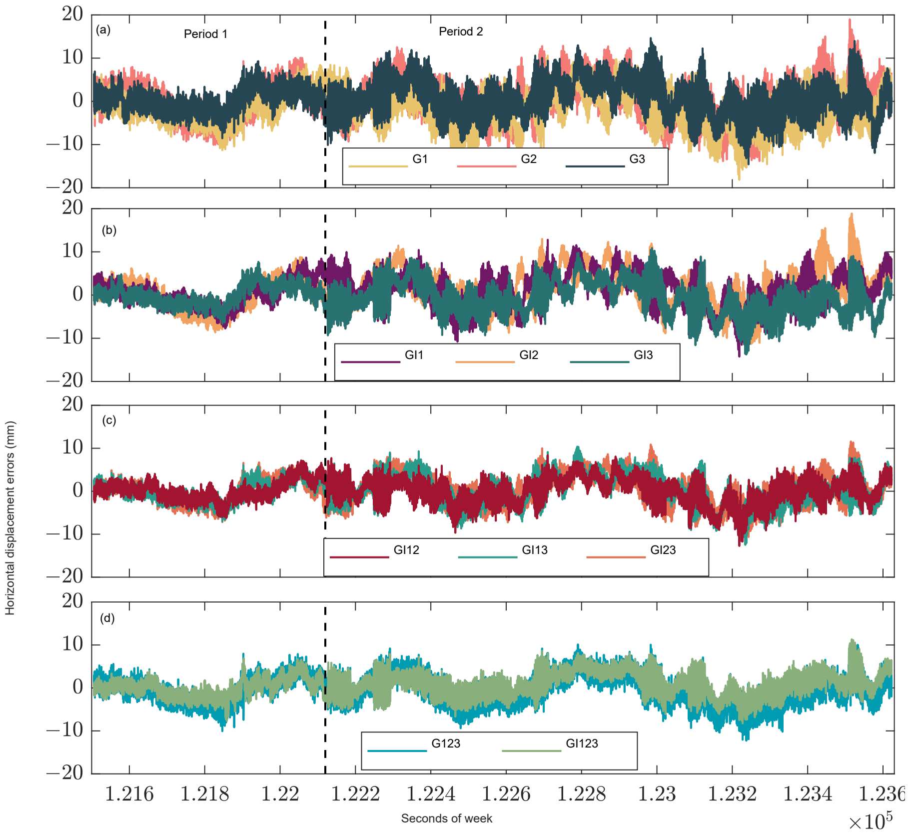

Figure 5. Horizontal displacement errors derived from (**a**) single-antenna GNSS-only, (**b**) single-antenna GNSS/IMU, (**c**) dual-antenna GNSS/IMU, and (**d**) triple-antenna GNSS-only and GNSS/IMU schemes.

Figure 6 shows the histograms of the displacement errors of different positioning schemes. For simplicity, only four typical schemes are shown (including G1, GI1, GI12, and GI123). We can see that the range of positioning errors of G1 is [−18.18, 10.59] mm, which is reduced to [−14.25, 12.79] mm when GNSS/IMU integration is adopted (i.e., GI1). When dual-antenna GNSS/IMU is used (i.e., GI12), the error range is further reduced to [−12.73, 8.38] mm. The triple-antenna GNSS/IMU solution achieves the best results, with the error range of [−8.24, 11.31] mm, and more errors are close to zero.

Table 3 presents the statistics of coordinate standard deviation errors (STDE) for all eleven positioning schemes. For the whole experiment period (including the static period and vibration period), the single-antenna GNSS-only positioning STDE is about 3.88 mm on average, with the STDEs of G1, G2, and G3 being 3.87, 4.21, and 3.57 mm, respectively. When the single-antenna GNSS is tightly integrated with IMU, the corresponding STDE only slightly declines to 3.73 mm (with the STDEs of GI1, GI2, and GI3 being 3.66, 4.12, and 3.41 mm respectively). We can find that the GNSS/IMU positioning performance is related to the positioning quality of the corresponding GNSS antenna used. This effect is less obvious when additional GNSS antennas are used in the integration. The positioning STDE is reduced to about 2.79–3.21 mm by applying dual-antenna GNSS/IMU integration, corresponding to an average accuracy improvement of 21.9% relative to the single-antenna GNSS-only solutions. The triple-antenna GNSS/IMU solution further increases the improvement rate to 33.0% by reducing the STDE to 2.60 mm. Moreover, we notice that the G123 solution is 10.6–24.2% more accurate than the single-antenna solutions (G1, G2, and

G3) by means of averaging, and GI123 further reduces the STDE, which is 18.5% smaller than that of G123. This confirms that the use of both IMU and multiple antennas contributes to the improvement in accuracy. As for the statistical results of Period 1 and Period 2, they are similar with those based on the whole data period, while the STDEs of Period 2 increase by about 0.6–1.5 mm compared with those of Period 1, mainly because of the influence of vibrations.

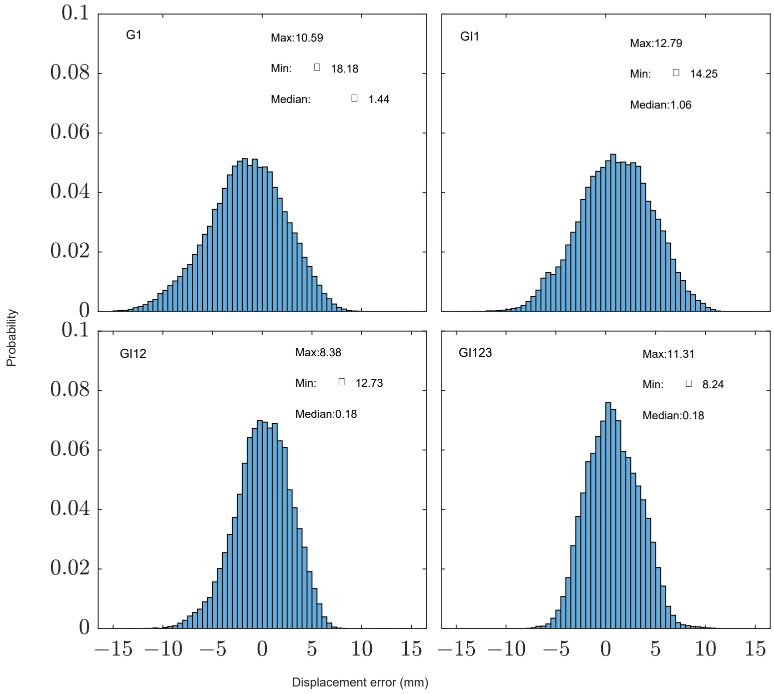

Figure 6. Histograms of displacement errors derived from four typical positioning schemes.

Table 3. Statistical results of 2D horizontal displacement errors of different positioning schemes.

Scheme	Period 1 and 2	Period 1	Period 2
	STDE/mm	STDE/mm	STDE/mm
G1	3.87	3.18	4.10
G2	4.21	3.75	4.36
G3	3.57	2.48	3.92
Mean	3.88	3.14	4.13
GI1	3.66	2.93	3.89
GI2	4.12	3.54	4.22
GI3	3.41	2.24	3.77
Mean	3.73	2.90	3.96
GI12	2.79	2.23	2.98
GI13	3.10	2.31	3.37
GI23	3.21	2.58	3.42
Mean	3.03	2.37	3.26
G123	3.19	2.75	3.35
GI123	2.60	2.08	2.73

Power spectral density (PSD) is calculated to analyze the spectrum of the displacement error sequences from the laser rangefinder and positioning schemes G1, GI1, GI12, and GI123 in the first four vibrations. The results of other positioning schemes, and other vibrations are similar, and thus, for brevity, they are not presented. As can be seen in Figure 7, all positioning schemes can successfully identify the main frequencies of the simulated vibrations, with numerically identical peak-frequency values with respect to those based on laser records. Despite this, compared to the PSD of laser records, the GNSS-only solution G1 is obviously noisier in the high-frequency band (e.g., >1 Hz). The GNSS/IMU solutions exhibit lower noise levels compared to G1, and integrating more GNSS antennas gradually enhances such improvement. This benefits the monitoring of vibrations with high frequencies and small amplitudes, which need further study. As for vibration amplitudes, we applied Fast Fourier Transform to estimate them. Figure 8 shows the errors of amplitudes estimated based on different positioning schemes: they are similar and mostly smaller than 3 mm; those of GI12 present the largest errors among the selected four schemes, perhaps due to the relatively poor data quality of Antenna 2.

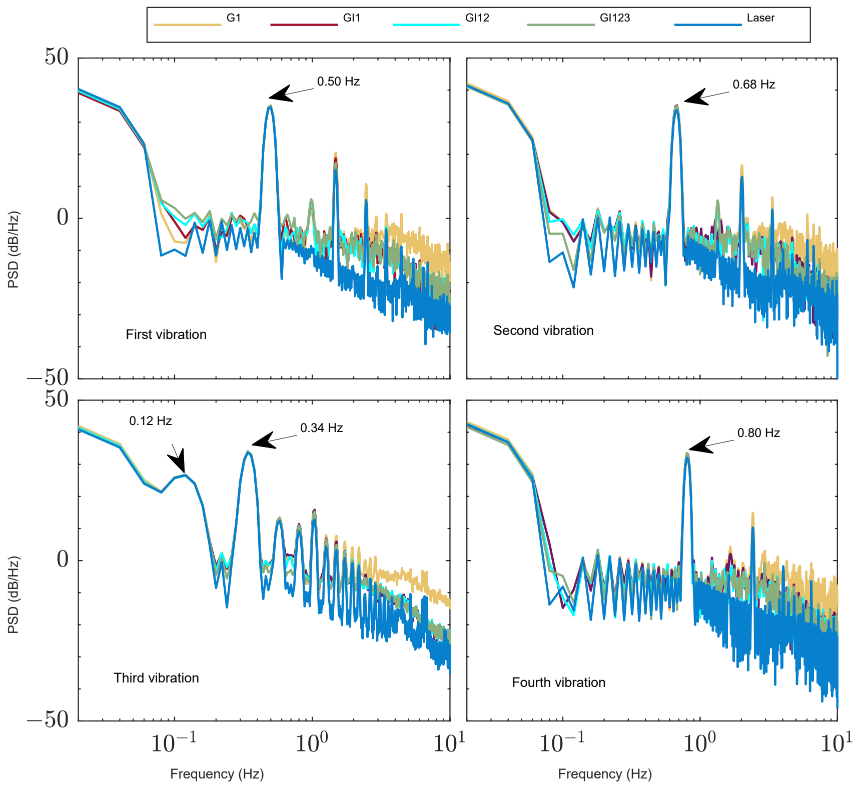

Figure 7. Power spectral density of displacements derived from different positioning schemes.

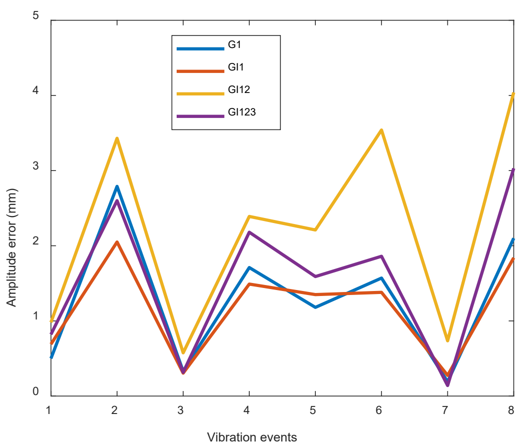

Figure 8. Errors of vibration amplitudes estimated based on displacements of different positioning schemes.

4. Conclusions

In SHM, GNSS can be limited due to signal interference and the accelerometers being subject to rotation-induced baseline errors. Traditional single-antenna GNSS/IMU integrations generally have low observation redundancy and model geometry strength. We propose a tightly integrated multi-antenna GNSS/IMU scheme for structural health monitoring. Vibration signals were simulated with a shaking table to validate the monitoring accuracy of the proposed method, using the laser rangefinder recordings as the reference.

Experimental results show that the STDEs of single-antenna GNSS-only solutions G1, G2, and G3 were 3.87, 4.21, and 3.57 mm, respectively. Compared to the results of single-antenna GNSS-only solutions, the single-antenna GNSS/IMU solutions are affected by the GNSS antenna used; thus, the positioning STDE was only slightly reduced from about 3.88 mm to 3.73 mm on average. Specifically, the STDEs of G1, G2, and G3 were 3.66, 4.12, and 3.41 mm, respectively. Adding more GNSS antennas can effectively increase the improvements. The dual-antenna GNSS/IMU integration reduces the STDE to a level of about 3.03 mm with the STDEs of GI12, GI13, and GI23 being 2.79, 3.10, and 3.21 mm, respectively, and positioning results with an STDE of 2.60 mm were finally obtained by triple-antenna GNSS/IMU integration, which is about 32.99%, 30.29%, and 14.19% more accurate than the single-antenna GNSS-only, single-antenna GNSS/IMU, and dual-antenna GNSS/IMU solutions, respectively. The power spectral density analysis demonstrates that vibration frequencies identified based on the displacements from different positioning schemes are nearly identical. Through Fast Fourier Transform analysis, we found that the benefit of integrating multi-antenna GNSS and IMU in estimating the vibration amplitudes is not obvious. This is perhaps because of the use of poor GNSS data from some antennas.

This study validates the effectiveness of the multi-antenna GNSS/IMU integrated model, and indicates the potential of multi-antenna GNSS/IMU integration for SHM. Further study may apply the proposed method in real SHM environments where more serious signal interference, such as occlusion, multipath, and diffraction errors, is generally present.

Author Contributions: Conceptualization, X.L. and W.Y.; methodology, X.L. and W.Y.; software, X.L. and W.Y.; validation, W.Y. and W.D.; formal analysis, X.L.; investigation, W.Y. and W.D.; data curation, X.Q. and X.D.; writing—original draft preparation, X.L.; writing—review and editing, W.Y. and W.D.; supervision, W.D.; funding acquisition, X.L., W.D., W.Y. and X.D. All authors have read and agreed to the published version of the manuscript.

Funding: This work was supported by the National Natural Science Foundation of China (Grant No. 42104022; 42388102); the Department of Natural Resources of Hunan Province (No. HNGTCH-2023-05); the Innovation and Technology Fund of Hong Kong (Project No. ITP/019/20LP); and the Fundamental Research Funds for the Central Universities of Central South University (Grant No. 2022ZZTS0474).

Data Availability Statement: The data presented in this study are available on request from the corresponding author.

Conflicts of Interest: The authors declare no conflicts of interest.

References

1. Ma, Z.; Choi, J.; Sohn, H. Structural displacement sensing techniques for civil infrastructure: A review. *J. Infrastruct. Intell. Resil.* **2023**, *2*, 100041. [CrossRef]
2. Sabato, A.; Dabetwar, S.; Kulkarni, N.N.; Fortino, G. Noncontact Sensing Techniques for AI-Aided Structural Health Monitoring: A Systematic Review. *IEEE Sens. J.* **2023**, *23*, 4672–4684. [CrossRef]
3. Zhang, C.; Mousavi, A.A.; Masri, S.F.; Gholipour, G.; Yan, K.; Li, X. Vibration feature extraction using signal processing techniques for structural health monitoring: A review. *Mech. Syst. Signal Proc.* **2022**, *177*, 109175. [CrossRef]
4. Tefera, B.; Zekaria, A.; Gebre, A. Challenges in applying vibration-based damage detection to highway bridge structures. *Asian J. Civ. Eng.* **2023**, *24*, 1875–1894. [CrossRef]

5. Braunfelds, J.; Senkans, U.; Skels, P.; Porins, J.; Haritonovs, V.; Spolitis, S.; Bobrovs, V. Development of the Strain Measurement Calibration Technique for Road Pavement Structural Health Monitoring Applications Using Optical FBG Sensors. In Proceedings of the 2023 Photonics & Electromagnetics Research Symposium (PIERS), Prague, Czech Republic, 3–6 July 2023; pp. 1060–1065. [CrossRef]
6. Sarmadi, H.; Entezami, A.; Yuen, K.; Behkamal, B. Review on smartphone sensing technology for structural health monitoring. *Measurement* **2023**, *223*, 113716. [CrossRef]
7. Entezami, A.; Arslan, A.N.; De Michele, C.; Behkamal, B. Online Hybrid Learning Methods for Real-Time Structural Health Monitoring Using Remote Sensing and Small Displacement Data. *Remote Sens.* **2022**, *14*, 3357. [CrossRef]
8. Wang, X.; Zhao, Q.; Xi, R.; Li, C.; Li, G.; Li, L. Review of Bridge Structural Health Monitoring Based on GNSS: From Displacement Monitoring to Dynamic Characteristic Identification. *IEEE Access* **2021**, *9*, 80043–80065. [CrossRef]
9. Tamura, Y.; Matsui, M.; Pagnini, L.; Ishibashi, R.; Yoshida, A. Measurement of wind-induced response of buildings using RTK-GPS. *J. Wind Eng. Ind. Aerodyn.* **2002**, *90*, 1783–1793. [CrossRef]
10. Nakamura, S. GPS Measurement of Wind-Induced Suspension Bridge Girder Displacements. *J. Struct. Eng.* **2000**, *126*, 1413–1419. [CrossRef]
11. Xiong, C.; Wang, M.; Chen, W. Data analysis and dynamic characteristic investigation of large-scale civil structures monitored by RTK-GNSS based on a hybrid filtering algorithm. *J. Civ. Struct. Health Monit.* **2022**, *12*, 857–874. [CrossRef]
12. Niu, Y.; Ye, Y.; Zhao, W.; Shu, J. Dynamic monitoring and data analysis of a long-span arch bridge based on high-rate GNSS-RTK measurement combining CF-CEEMD method. *J. Civ. Struct. Health Monit.* **2021**, *11*, 35–48. [CrossRef]
13. Stiros, S.C. Errors in velocities and displacements deduced from accelerographs: An approach based on the theory of error propagation. *Soil Dyn. Earthq. Eng.* **2008**, *28*, 415–420. [CrossRef]
14. Meng, X.; Wang, J.; Han, H. Optimal GPS/accelerometer integration algorithm for monitoring the vertical structural dynamics. *J. Appl. Geod.* **2014**, *8*, 265–272. [CrossRef]
15. Kim, K.; Choi, J.; Chung, J.; Koo, G.; Bae, I.; Sohn, H. Structural displacement estimation through multi-rate fusion of accelerometer and RTK-GPS displacement and velocity measurements. *Measurement* **2018**, *130*, 223–235. [CrossRef]
16. Xin, S.; Geng, J.; Zeng, R.; Zhang, Q.; Ortega-Culaciati, F.; Wang, T. In-situ real-time seismogeodesy by integrating multi-GNSS and accelerometers. *Measurement* **2021**, *179*, 109453. [CrossRef]
17. Sugisaki, K.; Abe, M.; Koshimizu, S. Inclination and vibration measurement by inertial sensing for structural health monitoring. *J. Jpn. Soc. Civ. Eng. A1* **2012**, *68*, 216–225. [CrossRef]
18. Sekiya, H.; Kinomoto, T.; Miki, C. Determination Method of Bridge Rotation Angle Response Using MEMS IMU. *Sensors* **2016**, *16*, 1882. [CrossRef] [PubMed]
19. Rossi, Y.; Tatsis, K.; Awadaljeed, M.; Arbogast, K.; Chatzi, E.; Rothacher, M.; Clinton, J. Kalman Filter-Based Fusion of Collocated Acceleration, GNSS and Rotation Data for 6C Motion Tracking. *Sensors* **2021**, *21*, 1543. [CrossRef]
20. de Alteriis, G.; Conte, C.; Caputo, E.; Chiariotti, P.; Accardo, D.; Cigada, A.; Schiano Lo Moriello, R. Low-Cost and High-Performance Solution for Positioning and Monitoring of Large Structures. *Sensors* **2022**, *22*, 1788. [CrossRef]
21. Geng, J.; Wen, Q.; Chen, Q.; Chang, H. Six-Degree-of-Freedom Broadband Seismogeodesy by Combining Collocated High-Rate GNSS, Accelerometers, and Gyroscopes. *Geophys. Res. Lett.* **2019**, *46*, 708–716. [CrossRef]
22. Cai, X.; Chai, H.; Ding, L.; Hsu, H.; Wang, Y. Multi-Antenna GNSS and INS Integrated Position and Attitude Determination without Base Station for Land Vehicles. *J. Navig.* **2019**, *72*, 342–358. [CrossRef]
23. Wang, Y.; Zhao, X.; Pang, C.; Feng, B.; Zhang, L. The Influence of Attitude Dilution of Precision on the Observable Degree and Observability Analysis with Different Numbers of Visible Satellites in a Multi-Antenna GNSS/INS Attitude Determination System. *IEEE Access* **2018**, *6*, 22156–22164. [CrossRef]
24. Li, X.; Zhou, Y.; Shen, Z.; Song, B.; Li, S. Using a Moving Antenna to Improve GNSS/INS Integration Performance under Low-Dynamic Scenarios. *IEEE Trans. Intell. Transp. Syst.* **2022**, *23*, 17717–17728. [CrossRef]
25. Lu, G. Development of a GPS Multi-Antenna System for Attitude Determination. Ph.D. Thesis, University of Calgary, Calgary, AB, USA, 1995. [CrossRef]
26. Zhang, Q.; Chen, Q.; Xu, Z.; Zhang, T.; Niu, X. Evaluating the navigation performance of multi-information integration based on low-end inertial sensors for precision agriculture. *Precis. Agric.* **2021**, *22*, 627–646. [CrossRef]
27. Li, Q.; Bai, Z.; Chen, B.; Guo, J.; Xin, H.; Chen, Y.; Li, Q.; Wu, F. A novel track measurement system based on GNSS/INS and multisensor for high-speed railway. *Acta Geod. Cartogr. Sin.* **2020**, *49*, 569–579. [CrossRef]
28. Groves, P. *Principles of GNSS, Inertial, and Multisensor Integrated Navigation Systems*, 2nd ed.; Industrial Robot; Artech: McLean, VA, USA, 2013; pp. 191–192.
29. Allan, D. Time and Frequency (Time-Domain) Characterization, Estimation, and Prediction of Precision Clocks and Oscillators. *IEEE Trans. Ultrason. Ferroelectr. Freq. Control* **1987**, *34*, 647–654. [CrossRef]